CHEMISTRY OF MATERIALS

pubs.acs.org/cm

Article

Oxide Ion Mobility in V- and P-doped Bi_2O_3-Based Solid Electrolytes: Combining Quasielastic Neutron Scattering with Ab Initio Molecular Dynamics

Bettina Schwaighofer, Miguel Angel Gonzalez,* Markus Appel, Michael Marek Koza, and Ivana Radosavljevic Evans*

Cite This: *Chem. Mater.* 2023, 35, 1125−1133

Read Online

ACCESS | Metrics & More | Article Recommendations | Supporting Information

ABSTRACT: We report the direct observation of oxide ion dynamics on both nano- and picosecond timescales in the isostructural Bi_2O_3-derived solid electrolytes $Bi_{0.852}V_{0.148}O_{1.648}$ and $Bi_{0.852}P_{0.148}O_{1.648}$ using quasielastic neutron scattering. Comprehensive ab initio molecular dynamics simulations allowed us to reproduce the experimental picosecond timescale data by directly simulating the scattering function at various temperatures. Our analysis of the experimental data in conjunction with the simulations revealed the origin of the picosecond dynamics to be localized motions within the V−O and P−O sublattices, while nanosecond dynamics correspond to the diffusion of the oxide ions in the Bi−O sublattice via vacancy-hopping. This combined approach provides insight into the different oxide ion migration pathways and mechanisms in $Bi_{0.852}V_{0.148}O_{1.648}$ and $Bi_{0.852}P_{0.148}O_{1.648}$, with the flexibility of the V coordination environment playing an important role, consistent with the superior conductivity of the vanadate.

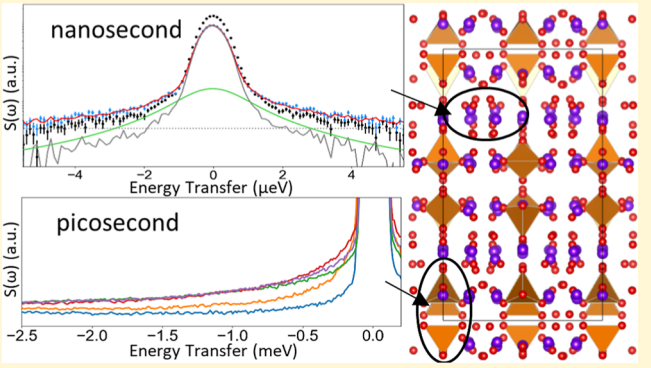

1. INTRODUCTION

Oxide ion conductors are important materials in applications like oxygen-permeable membranes and solid oxide fuel cells (SOFCs). In the latter, they are used as solid electrolytes. Current SOFC electrolyte materials, however, require high temperatures to achieve a sufficiently high oxide ion conductivity for device applications.[1] Developing materials with excellent ionic conductivity at intermediate temperatures (400−600 °C) is a crucial step in making SOFCs more widely applied. Understanding the relationships between structural properties and high ionic conductivity is therefore an important part of current research in this area of solid-state chemistry.

The cubic δ-phase of Bi_2O_3 is the best oxide ion conductor currently known, but it is only stable in a very narrow temperature range between 730 °C and the melting point at 817 °C.[2−4] Below that, it transforms into a monoclinic structure with a conductivity several orders of magnitude lower, making it unsuitable for applications. Isovalent or aliovalent substitution can stabilize the highly conductive phase at lower temperatures. Several such stabilizing dopants have been discovered, including Sr^{2+}, Nb^{5+}, Mo^{6+}, Er^{3+}, Dy^{3+}, W^{6+}, and Re^{7+}, but many of them transform into lower symmetry phases with a significantly lower conductivity after one or two heating cycles and are therefore not viable for applications.[4−12]

However, some of the most promising doped bismuth oxides are created by V^{5+}-doping.[13−16]

Two such materials are obtained by ∼9 and ∼15% V^{5+}-doping and have the formulae $Bi_{0.913}V_{0.087}O_{1.587}$ and $Bi_{0.852}V_{0.148}O_{1.648}$.[13,14] Generally, these materials can be described as consisting of two sublattices: a Bi−O sublattice and a V−O sublattice. The higher doping in $Bi_{0.852}V_{0.148}O_{1.648}$ disrupts the three-dimensional δ-Bi_2O_3-like sublattice present in $Bi_{0.913}V_{0.087}O_{1.587}$, resulting in a change in crystal structure from pseudo-cubic in $Bi_{0.913}V_{0.087}O_{1.587}$ to a monoclinic ordered fluorite superstructure in $Bi_{0.852}V_{0.148}O_{1.648}$.[13,14] A similar room temperature structure has been reported for the phosphorus analogue $Bi_{0.852}P_{0.148}O_{1.648}$, which has a P−O sublattice comparable to the V−O sublattice in the vanadate, with P and V atoms adopting tetrahedral coordination environments in isolated PO_4 and VO_4 groups, respectively.[15] Despite the isostructural nature of $Bi_{0.852}V_{0.148}O_{1.648}$ and $Bi_{0.852}P_{0.148}O_{1.648}$, their properties differ significantly, with the

Received: October 11, 2022
Revised: January 5, 2023
Published: January 18, 2023

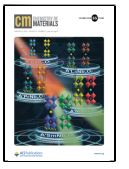

oxide ion conductivity of the vanadate being up to an order of magnitude higher in the temperature range of 300−600 °C.[14,16]

An initial ab initio molecular dynamics (AIMD) simulation[14] on $Bi_{0.852}V_{0.148}O_{1.648}$ suggested that, at elevated temperatures, the exchange of oxide ions between the Bi−O and V−O sublattices creates additional vacancies in the Bi−O sublattice, thereby assisting long-range O^{2-} diffusion. This is facilitated by the ability of V^{5+} to adopt variable coordination environments in VO_x groups (x = 4, 5, and 6). However, this simulation was very short (20 ps) and limited to one temperature (1373 K), which did not allow detailed, quantitative analysis of the localized and long-range dynamics.

Quasielastic neutron scattering (QENS) is an excellent technique for measuring diffusive processes. It allows determination of the geometry of the dynamics and has therefore been widely used to study proton conductors.[17,18] Its application for studying dynamics in oxide ion conductors, however, has been limited due to oxygen being an almost purely coherent neutron scatterer. The coherent QENS theory is less well developed and more complex, and combining this with the small neutron scattering cross section of oxygen and slower oxide ion dynamics compared to for example protons makes the analysis of the self-diffusion difficult.[18] AIMD calculations have previously shown good compatibility with QENS[19] and allow a more in-depth analysis of the experimental data; however, to the best of our knowledge, no attempt has been made to directly simulate the neutron scattering function of oxide ion conductors.

This paper aims to advance our understanding of ionic mobility in two very good solid electrolytes—isostructural $Bi_{0.852}V_{0.148}O_{1.648}$ and $Bi_{0.852}P_{0.148}O_{1.648}$ and demonstrate the ability of AIMD to directly simulate the neutron scattering observables of oxide ion conductors. To achieve this, QENS data were collected on two different timescales, and long (400 ps) AIMD simulations were performed at 500, 800, 950, 1100, 1250, and 1400 °C. QENS was measured on the nano- and picosecond timescales with the goal of probing dynamics in the two sublattices in each material separately. The results obtained from AIMD were then used to simulate the neutron scattering function at various temperatures. To the best of our knowledge, this is the first example providing quantitative analysis of QENS on two different timescales for oxide ion conductors. In addition to that, a comparative analysis of oxide ion dynamics in $Bi_{0.852}V_{0.148}O_{1.648}$ and previously reported $Bi_{0.913}V_{0.087}O_{1.587}$,[19] two materials with the same structural building blocks but different long-range structures, provides insight into the effect of different levels of doping on the conduction mechanism in Bi_2O_3-derived oxide ion conductors. $Bi_{0.852}V_{0.148}O_{1.648}$, $Bi_{0.852}P_{0.148}O_{1.648}$, and $Bi_{0.913}V_{0.087}O_{1.587}$ will be abbreviated as BVO-148, BPO-148, and BVO-087, respectively.

2. EXPERIMENTAL SECTION

2.1. Synthesis. Large (10 g) polycrystalline samples of BVO-148 and BPO-148 were prepared according to the previous literature[13,14,16] using stoichiometric amounts of Bi_2O_3 (Aldrich, 99.9% pure), V_2O_5 (Aldrich, >99.6% pure), and $(NH_4)H_2PO_4$ (Aldrich, >99.5% pure). The reagents were ground under isopropanol using an agate mortar and pestle and heated in open alumina crucibles at 700, 750, 800, and either 825 °C for $Bi_{0.852}V_{0.148}O_{1.648}$ or 850 °C for $Bi_{0.852}P_{0.148}O_{1.648}$ for 12 h at each temperature with intermitted grinding under isopropanol after each heating. To confirm sample purity, powder X-ray diffraction (PXRD) patterns were collected on a Bruker D8 ADVANCE diffractometer using Cu Kα radiation. The patterns were analyzed using the Rietveld method[20] implemented in Topas Academic.[21] The Rietveld fits demonstrating phase purity are given in the SI (Figure S1a,b).

2.2. Quasielastic Neutron Scattering. Neutron scattering data were collected on the time-of-flight spectrometer IN5 and the backscattering spectrometer IN16b at the Institut Laue-Langevin (ILL) in Grenoble.[22] The sample holder used was a cylindrical Nb can (diameter ∼ 8 mm, sample height ∼ 5 cm), which was placed in a furnace.[23]

For the IN5 experiment, an incident neutron wavelength of 4.8 Å giving a resolution of ∼86 μeV full width at half-maximum (FWHM) was used, providing insight into the fast (picosecond) dynamics. Data on BVO-148 were recorded for 2 h each at RT, 200, 400, 500, 600 °C, and on BPO-148 at 100 °C for 2 h, at 200 and 400 °C for 1 h each and at 500 and 600 °C for 4 h each. Data were also recorded on the empty Nb cell for 3.5 h and a vanadium sample for 30 min for data reduction. For the analysis, the room temperature data were used as the resolution.

On IN16b, the incident neutron wavelength was 6.271 Å and the instrument resolution was ∼0.8 μeV (FWHM), giving access to dynamics on a nanosecond timescale. On heating from room temperature to 600 °C for the vanadate and to 800 °C for the phosphate, elastic (E = 0 μeV) and inelastic (E = 2 μeV) scattered intensities were measured, so-called elastic and inelastic fixed window scans[24] (EFWS, IFWS), in steps of 25 K for 5 and 30 min, respectively. During this heating ramp, QENS measurements were performed at 25, 200, 400, 500, and 600 °C with collection times between 10 and 12 h per temperature, and an energy transfer window of ±7 μeV. Using the same energy transfer window, measurements were also performed on the empty Nb sample holder (2.5 h) for data reduction and analysis. The data from both IN5 and IN16b were reduced and analyzed using the Mantid[25] software.

2.3. Computational Methods. AIMD calculations were performed using the density functional theory method implemented in the Vienna Ab initio Simulation Package (VASP) code.[26] As a starting point, the structural models previously reported for $Bi_{0.852}V_{0.148}O_{1.648}$[14] and $Bi_{0.852}P_{0.148}O_{1.648}$,[15] transformed into $P1$ symmetry, were used. To preserve the nominal compositions while also ensuring full occupancy of all crystallographic sites in the simulation boxes, V and O atoms were removed using a random number generator, and likewise Bi and O from BPO-148, while maintaining a tetrahedral environment around the dopant cations. The atomic contents of the simulation boxes generated in this way were $Bi_{92}V_{16}O_{178}$ and $Bi_{92}P_{16}O_{178}$, in agreement with the nominal compositions. For all simulations, projector-augmented wave pseudopotentials[27] with the Perdew−Burke−Ernzerhof generalized-gradient-approximation functional[28] were used. The electronic structure was sampled at the gamma point only due to the large number of atoms in the simulation box. For both materials, AIMD calculations were performed at 500, 800, 950, 1100, 1250, and 1400 °C in the *NVT* ensemble, using a time step of 2 fs and a cutoff energy of 400 eV to simulate a total of 400 ps per temperature for each material. The data analysis was carried out using the MDANSE code.[29]

3. RESULTS AND DISCUSSION

3.1. Nanosecond Dynamics in BVO-148 and BPO-148. Figure 1 shows the IFWS for BVO-148 and BPO-148 collected on IN16b,[24] which were corrected for the sample can contributions as well as residual elastic contribution. These scans measure the inelastic intensity at a defined energy offset close to the elastic peak (±2 μeV) as a function of temperature. The onset of dynamics in a system causes a broadening of the elastic peak (QENS signal), resulting in an increase in inelastic intensity at the chosen energy offset. Therefore, IFWS can be used to estimate in which temperature range the systems dynamics can be observed as the wing of the

https://doi.org/10.1021/acs.chemmater.2c03103
Chem. Mater. 2023, 35, 1125−1133

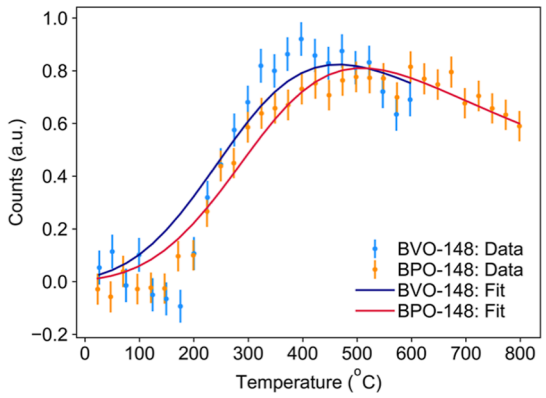

Figure 1. Plots of the IFWS intensity measured at 2 μeV and summed over all measured Q as a function of temperature, showing maxima at 420 °C for BVO-148 and 500 °C for BPO-148 according to the fits (shown as solid lines), indicating that QENS broadening can be observed in this temperature range for both materials. For BVO-148, the activation energy obtained from QENS (0.18 eV, see below) was used for fitting.

quasielastic signal reaches the fixed observation energy, or becomes too broad with respect to that energy.

The IFWS were corrected for elastic contamination by subtracting the rescaled elastic intensity. The small decrease in inelastic intensity below 200 °C for BVO-148 seen in Figure 1 is caused by elastic leakage, which could not be fully corrected for in this subtraction. There is a clear increase in inelastic intensity at 200 °C as the dynamics enter the measured energy transfer window. This results in a broad maximum at around 420 °C for BVO-148 and 500 °C for BPO-148 (Figure 1). At higher temperatures, faster dynamics lead to a decrease in the IFWS intensity as the QENS broadening becomes larger than the observed energy transfer window.

The IFWS can be fitted by assuming an Arrhenius-type behavior of the relaxation time.[24] This allows for the activation energy of the observed dynamic process to be determined, giving a value of 0.20 ± 0.01 eV for BPO-148, as shown in the red fit in Figure 1. For BVO-148, the activation energy obtained from QENS (0.18 eV, see below) was used, and the good fit as shown in Figure 1 confirms that both the IFWS and QENS probe the same process. Considering the isostructural nature of BVO-148 and BPO-148 as well as the good agreement of the onset temperatures and activation energies of the dynamics, we conclude that the same type of dynamics is measured in both compounds.

The Q-dependence of the IFWS is shown in Figure S2 and provides additional information on the diffusive process. The Arrhenius prefactor which describes the linewidth at an infinite temperature of both materials appears constant within the accessed Q-range, indicating that the observed dynamics are primarily localized.[24]

Plots of the scattering function $S(\omega)$ at room temperature and at 400 °C for BVO-148 and BPO-148 are shown in Figure 2. The neutron scattering cross section of oxygen is moderate and fully coherent, which generally means that the observed QENS broadening is small, making the analysis of experimental results challenging. Therefore, data were summed over selected detectors in which the broadening was most apparent, covering a Q-range of 1.39 to 1.74 Å^{-1}. The QENS signal is significantly weaker than that reported for the pseudo-cubic BVO-087,[19] which is consistent with impedance data showing the lower

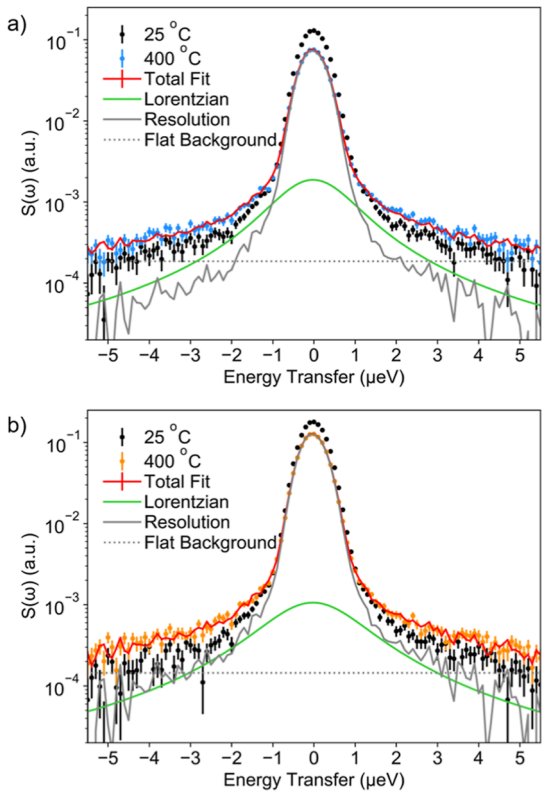

Figure 2. Total scattering function $S(\omega)$ of (a) BVO-148 and (b) BPO-148 measured on IN16b at room temperature and at 400 °C. Fits of the 400 °C data using eq 1, showing the different contributions. The data have been summed over the detectors, where the broadening was clearest, covering a Q-range from 1.39 to 1.74 Å^{-1}.

conductivity of the monoclinic materials BVO-148 and BPO-148.[14,16] The Q-integrated scattering function $S(\omega)$ was fitted as shown by eq 1, using a single Lorentzian function $\mathcal{L}$ of FWHM Γ and amplitude A, and a delta function $\delta(\omega)$ of height h, whose sum was then convoluted with the resolution function $R(\omega)$. A flat background B was also added.

$$S(\omega) = R(\omega) \otimes [h\delta(\omega) + A\mathcal{L}(\Gamma, \omega)] + \mathrm{B} \quad (1)$$

The FWHM of the Lorentzian has an Arrhenius-type relationship to the activation energy of the process causing the broadening,[30] and could be extracted at three temperatures for the vanadate (Figure 3), giving an activation energy of 0.18 ± 0.04 eV. For BPO-148, some broadening at 400 °C could also be observed, as shown in Figure 2b, but due to the weak temperature dependence of the dynamics above 400 °C, no activation energy from QENS could be extracted. The activation energy found for BVO-148 is in good agreement with that of 0.16 ± 0.02 eV found by ^{17}O T1 relaxation measurements from solid-state NMR for dynamics in the Bi−O sublattice, which the authors ascribed to nearest neighbor vacancy jumps.[31]

Despite impedance data showing significant ionic conductivity for BVO-148 in the measured temperature range,[14] this long-range diffusion is likely too slow to fall completely within the timescale probed by IN16b, meaning that the nanosecond dynamics observed in this study on BVO-148 and BPO-148 are predominantly local nearest neighbor jumps.

3.2. Picosecond Dynamics in BVO-148 and BPO-148.

To obtain a more complete insight into the dynamics, one

https://doi.org/10.1021/acs.chemmater.2c03103
Chem. Mater. 2023, 35, 1125−1133

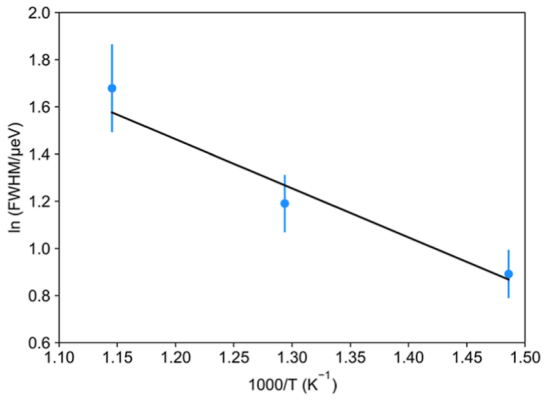

Figure 3. Arrhenius-type plot of the FWHM (μeV) obtained from fitting the IN16b data at various temperatures for BVO-148.

which can be directly compared to the AIMD calculations (Section 3.3), we performed measurements probing the picosecond timescale on IN5. Simple temperature effects were taken into account by normalizing the experimental spectra by the Debye−Waller and Bose population factors. The resulting curves, exhibiting a clear quasielastic broadening with increasing temperature, are shown in Figure 4.

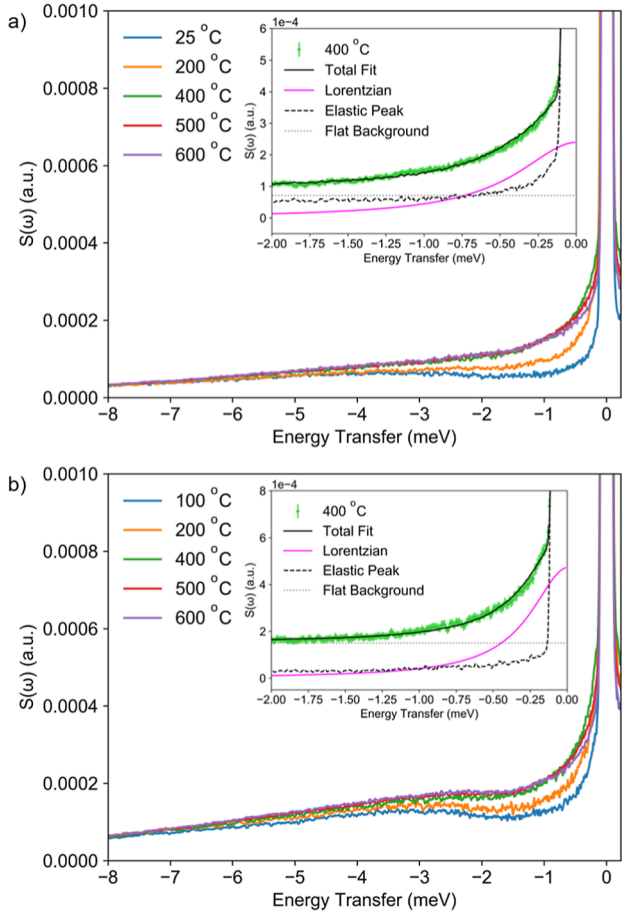

Figure 4. $S(\omega)$ of (a) BVO-148 and (b) BPO-148 collected on IN5 at various temperatures and summed over Q = 1.6−1.8 Å^{-1}. The insets show the fit of the data at 400 °C using a convolution of the resolution with a delta function for the elastic peak and a Lorentzian for the QENS signal.

This observation is in contrast with the results previously obtained for BVO-087, where measurements performed on the IN6 spectrometer did not show any observable dynamics on the picosecond time scale.[19] In that case, the authors hypothesized that either the local dynamics take place on a different time scale to that of IN6 or that the signal was too weak to be observed. In our present study, the higher V-doping results in a larger number of oxide ions moving in the V−O sublattice, causing a larger signal. Additionally, the experimental setup (better resolution of purely Gaussian shape) in our current investigation compared to the one used previously on BVO-087[19] facilitates the observation of a small QENS signal in the meV range (Figure 4).

The complex fluorite superstructures in which BVO-148 and BPO-148 crystallize lead to Bragg peaks in large parts of the measured Q-range, as shown in Figure S3. In addition to that, below 0.8 Å^{-1} the signal was too weak to be fitted. Therefore, to analyze the temperature dependence of the elastic broadening, only data in the Q-range of 1.6−1.8 Å^{-1} were summed and used for fitting. A plot of Lorentzian linewidth against temperature for BVO-148 and BPO-148 is shown in Figure 5. The extracted activation energies are 0.083 ± 0.009 and 0.030 ± 0.004 eV for the vanadate and phosphate, respectively.

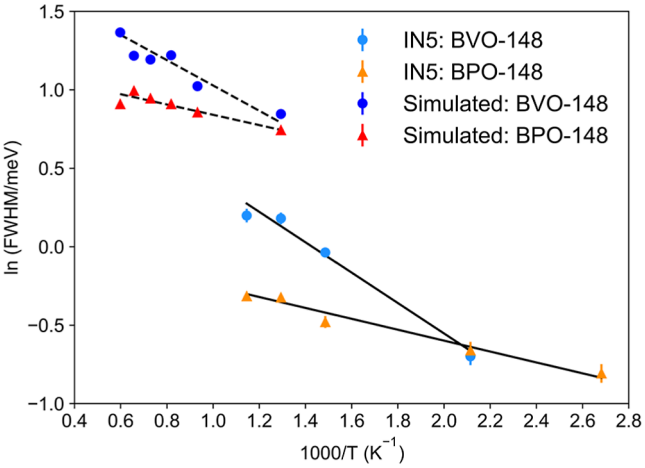

Figure 5. Arrhenius-type plot of the FWHM (meV) obtained from fitting experimental IN5 $S(\omega)$ data and simulated $S(\omega)$, both summed over a Q-range of 1.6−1.8 Å^{-1}, giving the activation energy of the picosecond dynamics observed on IN5 and from AIMD simulations, respectively.

These values are in excellent agreement with NMR data for motions in the V−O (0.06 ± 0.02 eV) and P−O (0.04 ± 0.02 eV) sublattices,[31] as well as with the small activation barriers of 0.05−0.07 eV previously reported for other tetrahedral species like MnO_4^- and SO_4^{2-}.[32,33] We, therefore, conclude that the dynamics we observe on IN5 are localized motions of O atoms within the VO_x and PO_4 polyhedra; similar flexibility of the VO_x polyhedra has also been reported for Sr-doped $BiVO_4$.[34] The activation energy of rotation of VO_x polyhedra determined from IN5 data is higher than that for rotation of PO_4. One explanation for this could be the on average shorter P−O bond length compared to V−O. Typical bond lengths in VO_4 and VO_5 polyhedra are 1.72 and 1.82 Å respectively,[35] and the typical bond length in PO_4 is 1.53 Å.[35] This leads to PO_4 tetrahedra being smaller compared to VO_x polyhedra,

https://doi.org/10.1021/acs.chemmater.2c03103
Chem. Mater. 2023, 35, 1125−1133

resulting in shorter O−O distances and therefore a lower activation energy for jumps between oxygen sites on the apices of the coordination polyhedra.

3.3. AIMD Simulations of Oxide Ion Dynamics in BVO-148 and BPO-148. While the direct observation of dynamics with QENS generally allows for a very detailed analysis of different motions in ionic conductors, this is severely limited for oxide ion conductors due to the relatively small and fully coherent character of the neutron scattering cross section of oxygen. Additionally, in structurally complex materials like the ones investigated here, the presence of Bragg peaks makes the analysis of the Q-dependence of the QENS signal extremely difficult or even impossible. AIMD calculations have previously been used to gain a better understanding of the observed dynamics and show good compatibility with QENS.[14,19,36−38] More specifically, a combined QENS and AIMD approach has been used to elucidate the oxide ion diffusion mechanism in a number of structurally complex materials, for example, $Bi_{26}Mo_{10}O_{69}$,[7] $La_2Mo_2O_9$,[37] and $Bi_{0.913}V_{0.087}O_{1.587}$,[19] by allowing a detailed insight into local motions and jumps which result in long-range dynamics.

Preliminary AIMD simulations[14] suggested that the average coordination number (CN) of V in BVO-148 increases during the simulation at elevated temperatures as a result of oxide ions diffusing from the Bi−O sublattice into the V−O sublattice. A recent solid-state NMR study[31] suggested an increase in oxide ion exchange between the Bi−O and V−O sublattices with increasing temperatures for BVO-087 and BVO-148, but only very limited exchange in BPO-148. This structural aspect was addressed by our AIMD simulations. Figure 6 depicts the

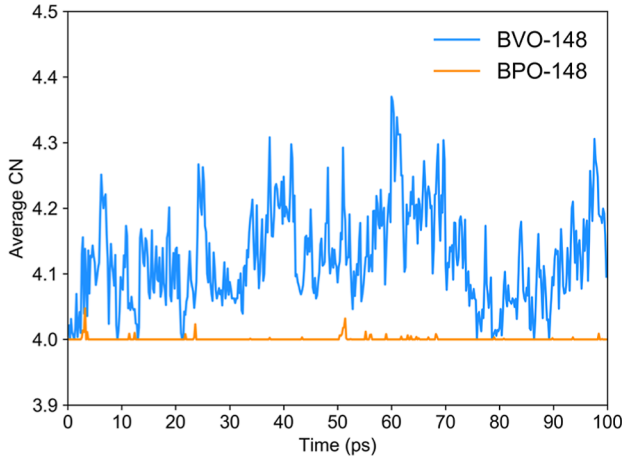

Figure 6. Average CN of V in BVO-148 and P in BPO-148 derived from AIMD simulations at 1100 °C.

average CN of all V and P atoms in the simulation boxes at 1100 °C during the first 100 ps of the simulation, showing that the coordination environment of V varies significantly. The average CN is 4.13, corresponding to 2 out of 16 V being 5-coordinate and reaches a maximum of 4.37, where 6 out of 16 V are 5-coordinate. In contrast to that, the average CN of P is 4.00, showing that P essentially remains tetrahedral.

In doped bismuth oxides, migration of oxide ions into the dopant sublattice creates additional vacancies in the Bi−O sublattice.[13,19] An increase in this hopping rate with temperature, therefore, results in faster dynamics in the Bi−O sublattice. In contrast, there is only limited oxide ion exchange in BPO-148, as shown by our simulations. This directly shows the importance of a dopant that readily adopts various coordination environments to achieve faster dynamics and therefore a high conductivity.[5,14,19,37,39]

To allow a direct comparison of AIMD to experimental data, $S(\omega)$ was simulated using the resolution of IN5 at 4.8 Å and various temperatures and fitted as shown in Figure S4 using eq 1. Activation energies of 0.069 ± 0.008 eV for the vanadate and 0.028 ± 0.004 eV for the phosphate were obtained from the temperature dependence of the Lorentzian FWHM (Figure 5).

Due to the presence of inelastic features at low energy transfers, the experimental data were fitted over a narrow energy range. In the simulated data, this could be included in the fit, allowing fitting over a larger energy range. This improves the quality of the fit and helps explain the difference between the experimental and simulated FWHM, which is apparent in Figure 5. Nevertheless, the temperature dependence of the QENS signal is reproduced well, and the excellent agreement of experimental and simulated activation energies confirms that we observe the same dynamics in both methods. This validates the simulations, warranting their further, in-depth analysis.

First, it allows the extraction of the elastic incoherent structure factor (EISF), a parameter which, due to the essentially purely coherent scattering nature of oxygen, is not obtainable from experiments. It can be related to the space accessible to scattering atoms for localized motions, thereby providing information about the geometry of the dynamics.[40] The EISF was extracted from the value of the simulated self-intermediate scattering function for oxygen at 500 °C and 300 ps. For this purpose, oxygen atoms were grouped into two categories depending on the sublattice in which they originated at the start of the simulation, that is, V/P−O and Bi−O.

Figure 7 shows the EISF of the oxygen atoms in the V−O and P−O sublattices corrected by the Debye−Waller factor,[41]

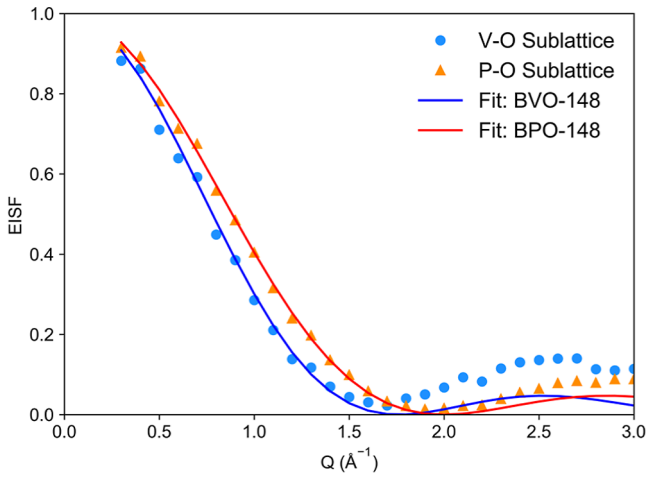

Figure 7. Simulated EISF, showing localized motion in the V−O and P−O sublattices in BVO-148 and BPO-148, which can be fitted with the diffusion on the surface of a sphere model.

using the mean-square displacement (MSD) obtained from the EISF of Bi. Fitting of the EISF shows that the dynamics on the picosecond timescale can be reasonably approximated by a model of diffusion on the surface of a sphere[40] in both BVO-148 and BPO-148. For a uniform diffusion over the sphere, the EISF is given by

https://doi.org/10.1021/acs.chemmater.2c03103
Chem. Mater. 2023, 35, 1125−1133

$$\mathrm{EISF} = \left(\frac{\sin(QR)}{QR}\right)^2 \quad (2)$$

where Q is the momentum transfer, and R is the radius of the sphere. The fit of this simple model to the AIMD-derived EISF is shown in Figure 7.

The model reproduces the data below the minimum very well, while some deviations at larger Q values are observed. This is not surprising, as we do not expect the VO_x/PO_4 polyhedron to define a perfectly spherical surface. In addition to that, preferential orientations in some particular crystallographic directions will also result in deviations from the ideal isotropic spherical model. Nevertheless, the fit of eq 2 to the simulated EISF gives an estimate of the average rotational radii of 1.78 ± 0.04 and 1.57 ± 0.02 Å for the vanadate and phosphate, respectively, which are in very good agreement with known V−O and P−O distances.

The simulation time of 400 ps was not long enough to simulate IN16b data, which probes a timescale of several nanoseconds. The MSDs can nevertheless give reliable information about the long-range dynamics. The MSD curves for all oxygen atoms at 500 and 1100 °C for both materials are shown in Figure 8a. At 500 °C, the MSD curves corresponding to the oxide ions in both materials reach a constant value after a few ps. There are no signs of long-range diffusion; therefore, the dynamics observed at this temperature are localized motions within the VO_x/PO_4 polyhedra. These relatively fast local motions are the origin of the simulated EISF shown in Figure 7, as well as the QENS broadening observed in the meV regime in both, the experimental and simulated spectra.

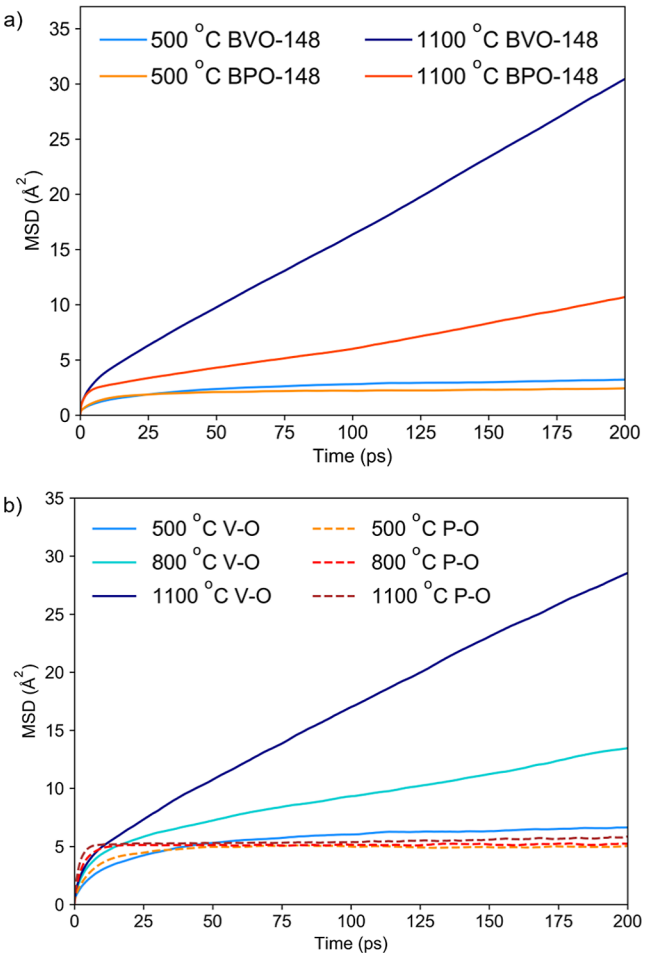

Figure 8. MSD curves (a) for all oxygen atoms at 500 and 1100 °C and (b) for oxygen atoms initially in the V−O or P−O sublattice at 500, 800, and 1100 °C.

At 1100 °C, the MSDs increase without plateauing, showing the presence of long-range dynamics in BVO-148 and BPO-148. The average MSD at all temperatures is higher in the vanadate than the phosphate, consistent with higher conductivity.[14,16] Again, to gain a better understanding of the effect of the dopant on long-range diffusion, oxygen atoms were separated into V/P−O and Bi−O oxygen atoms depending on their original sublattice. A direct comparison of the MSDs of oxygen atoms in the V−O and the P−O sublattices can be seen in Figure 8b. At 500 °C, the plots for both compounds show a clear plateau, indicating predominantly localized diffusion at this temperature, as discussed previously. As the temperature increases, a difference in the dynamics in the two materials becomes more pronounced, highlighting the difference in the conduction mechanism in BVO-148 and BPO-148.

The MSDs of oxygen atoms in the P−O sublattice suggest largely localized motions even at 1100 °C, indicating that ionic conductivity is dominated by the diffusion of Bi−O oxygen atoms, with little contribution from the P−O sublattice. In contrast to that, the MSD curves of oxygen atoms initially within the V−O sublattice show no sign of saturation at 800 °C and above due to the rapid exchange between sublattices at increased temperatures in BVO-148.

The slope of the MSD curves can be used to determine the diffusion coefficients, D, which can then be used to calculate the activation energy for long-range diffusion. Figure 9 shows

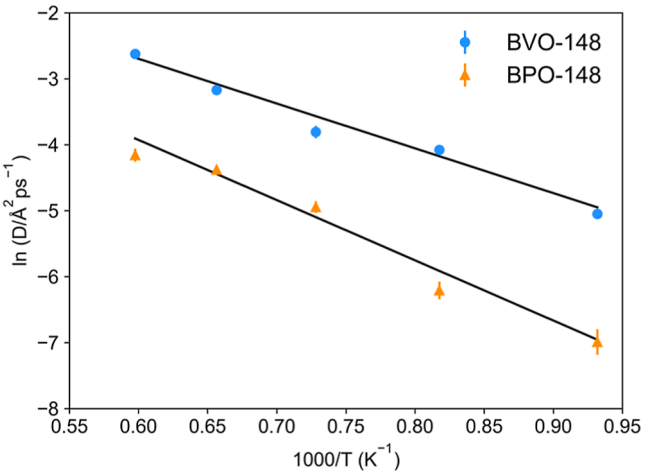

Figure 9. Arrhenius-type plot of diffusion coefficients against inverse temperature for BVO-148 and BPO-148.

the self-diffusion coefficient determined from the behavior of the MSD of all oxygen atoms. The obtained activation energies are 0.60 ± 0.05 and 0.77 ± 0.07 eV for the vanadate and phosphate, respectively. This is slightly lower than values determined from impedance data (0.73 eV for BVO-148[14] and 0.85 eV for BPO-148[16]), a type of discrepancy which has often been found when comparing data from microscopic methods like AIMD simulations or NMR to impedance spectroscopy.[19,37,42−45] However, the higher activation energy of BPO-

https://doi.org/10.1021/acs.chemmater.2c03103
Chem. Mater. 2023, 35, 1125−1133

148 compared to BVO-148 is reproduced well, further validating the AIMD simulations.

Examining the diffusion coefficients at 800 °C directly gives further insights into the long-range dynamics. The determined values are 9.5×10^{-7} cm^2 s^{-1} for BVO-148 and 0.6×10^{-7} cm^2 s^{-1} for BPO-148, reflecting the inferior conductivity of the phosphate. Comparison to the value of pure δ-Bi_2O_3 at the same temperature,[36] 1.7×10^{-5} cm^2 s^{-1}, is consistent with the disruption of the Bi−O sublattice and the change from a cubic to a monoclinic structure decreasing conductivity. For BVO-087, the highest simulation temperature of 600 °C,[19] gives a diffusion coefficient of around 5×10^{-7} cm^2 s^{-1}, comparable to that of BVO-148 at 800 °C, showing that long-range dynamics are significantly faster in the former. This faster diffusion in BVO-087 supports the conclusions drawn from IN16b data, explaining why long-range motion could be observed in the previous study of BVO-087 but was outside the timescale covered by IN16b for BVO-148.

4. CONCLUSIONS

QENS has been used successfully to investigate both nano- and picosecond dynamics in BVO-148 and BPO-148. This is the first time a quantitative analysis of QENS on two different timescales was possible for oxide ion conductors and allowed a separation of dynamics in the Bi−O sublattices and the dopant sublattices for both materials.

Experiments on IN16b revealed nanosecond dynamics in the Bi−O sublattices of both the vanadate and phosphate. The activation energies obtained suggest that these dynamics are primarily short-range, and while they can be expected to directly influence bulk ionic conductivity, access to longer timescales is needed to observe long-range diffusion in BVO-148 and BPO-148 directly.

IN5 measurements allowed direct observation of localized motions on a picosecond timescale in the dopant sublattices of BVO-148 and BPO-148 caused by fast reorientations of the VO_x and PO_4 polyhedra, with respective activation energies of 0.083 ± 0.009 and 0.030 ± 0.004 eV.

Using very long AIMD simulations of BVO-148 and BPO-148 at various temperatures enabled us to simulate the scattering functions $S(Q,\omega)$, allowing a direct comparison of the AIMD results to experimental data. The activation energies obtained from the temperature dependence of the simulated $S(\omega)$, 0.069 ± 0.008 eV for the vanadate and 0.028 ± 0.004 eV for the phosphate, are in excellent agreement with those obtained from experimental data. This validates the simulations, rationalizing a more in-depth analysis, which is particularly beneficial for complex, coherently scattering systems like oxide ion conductors. The simulated EISF was used to confirm the geometry of the picosecond dynamics, which was not possible from experimental data alone.

Activation energies for the long-range diffusion obtained from simulated MSD plots at various temperatures agree well with previously reported impedance data.[14,16] Additionally, the MSD plots show a strong correlation of dynamics between the dopant sublattice and the Bi−O sublattice in BVO-148 at increasing temperatures due to fast oxide ion exchange, while the very limited exchange in BPO-148 results in predominantly localized motions of oxygen atoms in the P−O sublattice.

In conclusion, with regards to the design of improved oxide ion conductors, the comparison of BVO-148 and BPO-148 underlines the importance of using dopants which can adopt various coordination environments and thereby create more vacancies in the Bi−O sublattice, enhancing the conductivity. Moreover, a direct comparison of QENS data and AIMD simulations for oxide ion conductors presented here emphasizes the compatibility of these two methods and demonstrates the potential of AIMD to aid in the analysis of coherent QENS data.

■ ASSOCIATED CONTENT

Supporting Information

The Supporting Information is available free of charge at https://pubs.acs.org/doi/10.1021/acs.chemmater.2c03103.

Diffraction patterns of the synthesized compounds from PXRD; Arrhenius prefactor of the fixed window scans obtained on IN16b; diffraction patterns obtained from neutron scattering experiments on IN5; and fit of simulated $S(\omega)$ (PDF)

■ AUTHOR INFORMATION

Corresponding Authors

Miguel Angel Gonzalez − *Institut Laue Langevin, 38042 Grenoble, France*; Email: gonzalezm@ill.fr

Ivana Radosavljevic Evans − *Department of Chemistry, Durham University, Durham DH1 3LE, U.K.*; orcid.org/0000-0002-0325-7229; Email: ivana.radosavljevic@durham.ac.uk

Authors

Bettina Schwaighofer − *Department of Chemistry, Durham University, Durham DH1 3LE, U.K.; Institut Laue Langevin, 38042 Grenoble, France*; orcid.org/0000-0002-2151-169X

Markus Appel − *Institut Laue Langevin, 38042 Grenoble, France*

Michael Marek Koza − *Institut Laue Langevin, 38042 Grenoble, France*

Complete contact information is available at: https://pubs.acs.org/10.1021/acs.chemmater.2c03103

Notes

The authors declare no competing financial interest.

■ ACKNOWLEDGMENTS

The authors thank Institut Laue Langevin and Durham University for PhD funding for B.S. We also acknowledge Institut Laue Langevin for the allocation of neutron beamtime which provided the experimental data underlying this study (available under doi: 10.5291/ILL-DATA.7-03-184) and the allocation of computer resources through the C-lab. We thank Professor Mark Johnson (ILL) for the useful discussions.

■ REFERENCES

(1) Steele, B. C. H.; Heinzel, A. Materials for Fuel-Cell Technologies. *Nature* **2001**, *414*, 345−352.

(2) Harwig, H. A.; Gerards, A. G. Electrical Properties of the α, β, γ, and δ Phases of Bismuth Sesquioxide. *J. Solid State Chem.* **1978**, *26*, 265−274.

(3) Battle, P. D.; Catlow, C. R. A.; Drennan, J.; Murray, A. D. The Structural Properties of the Oxygen Conducting δ Phase of Bi_2O_3. *J. Phys. C: Solid State Phys.* **1983**, *16*, L561−L566.

(4) Takahashi, T.; Iwahara, H. Oxide Ion Conductors Based on Bismuthsesquioxide. *Mater. Res. Bull.* **1978**, *13*, 1447−1453.

(5) Payne, J. L.; Farrell, J. D.; Linsell, A. M.; Johnson, M. R.; Evans, I. R. The Mechanism of Oxide Ion Conductivity in Bismuth Rhenium Oxide, $Bi_{28}Re_2O_{49}$. *Solid State Ionics* **2013**, *244*, 35−39.
(6) Tate, M. L.; Hack, J.; Kuang, X.; McIntyre, G. J.; Withers, R. L.; Johnson, M. R.; Evans, I. R. $Bi_{1-x}Nb_xO_{1.5+x}$ (x=0.0625, 0.12) Fast Ion Conductors: Structures, Stability and Oxide Ion Migration Pathways. *J. Solid State Chem.* **2015**, *225*, 383−390.
(7) Ling, C. D.; Miiller, W.; Johnson, M. R.; Richard, D.; Rols, S.; Madge, J.; Evans, I. R. Local Structure, Dynamics, and the Mechanisms of Oxide Ionic Conduction in $Bi_{26}Mo_{10}O_{69}$. *Chem. Mater.* **2012**, *24*, 4607−4614.
(8) Goodenough, J. B. Oxide-Ion Electrolytes. *Annu. Rev. Mater. Res.* **2003**, *33*, 91−128.
(9) Jiang, N.; Wachsman, E. D.; Jung, S. A Higher Conductivity Bi_2O_3-Based Electrolyte. *Solid State Ionics* **2002**, *150*, 347−353.
(10) Park, J. Y.; Wachsman, E. D. Stable and High Conductivity Ceria/Bismuth Oxide Bilayer Electrolytes for Lower Temperature Solid Oxide Fuel Cells. *Ionics* **2006**, *12*, 15−20.
(11) Punn, R.; Feteira, A. M.; Sinclair, D. C.; Greaves, C. Enhanced Oxide Ion Conductivity in Stabilized δ-Bi_2O_3. *J. Am. Chem. Soc.* **2006**, *128*, 15386−15387.
(12) Hervoches, C. H.; Greaves, C. Crystal Structure and Oxide Ion Conductivity in Cubic (Disordered) and Tetragonal (Ordered) Phases of $Bi_{25}Ln_3Re_2O_{49}$ (Ln = La, Pr). *J. Mater. Chem.* **2010**, *20*, 6759−6763.
(13) Kuang, X.; Payne, J. L.; Johnson, M. R.; Evans, I. R. Remarkably High Oxide Ion Conductivity at Low Temperature in an Ordered Fluorite-Type Superstructure. *Angew. Chem., Int. Ed.* **2012**, *51*, 690−694.
(14) Kuang, X.; Payne, J. L.; Farrell, J. D.; Johnson, M. R.; Evans, I. R. Polymorphism and Oxide Ion Migration Pathways in Fluorite-Type Bismuth Vanadate, $Bi_{46}V_8O_{89}$. *Chem. Mater.* **2012**, *24*, 2162−2167.
(15) Darriet, J.; Launay, J. C.; Zúniga, F. J. Crystal Structures of the Ionic Conductors $Bi_{46}M_8O_{89}$ (M=P, V) Related to the Fluorite-Type Structure. *J. Solid State Chem.* **2005**, *178*, 1753−1764.
(16) Watanabe, A. $Bi_{23}M_4O_{44.5}$ (M = P and V): New Oxide-Ion Conductors with Triclinic Structure Based on a Pseudo-Fcc Subcell. *Solid State Ionics* **1997**, *96*, 75−81.
(17) Karlsson, M. Proton Dynamics in Oxides: Insight into the Mechanics of Proton Conduction from Quasielastic Neutron Scattering. *Phys. Chem. Chem. Phys.* **2014**, *17*, 26−38.
(18) Coduri, M.; Karlsson, M.; Malavasi, L. Structure-Property Correlation in Oxide-Ion and Proton Conductors for Clean Energy Applications: Recent Experimental and Computational Advancements. *J. Mater. Chem. A* **2022**, *10*, 5082−5110.
(19) Peet, J. R.; Fuller, C. A.; Frick, B.; Koza, M. M.; Johnson, M. R.; Piovano, A.; Evans, I. R. Insight into Design of Improved Oxide Ion Conductors: Dynamics and Conduction Mechanisms in the $Bi_{0.913}V_{0.087}O_{1.587}$ Solid Electrolyte. *J. Am. Chem. Soc.* **2019**, *141*, 9989−9997.
(20) Rietveld, H. M. A Profile Refinement Method for Nuclear and Magnetic Structures. *J. Appl. Crystallogr.* **1969**, *2*, 65−71.
(21) Coelho, A. A.; Evans, J.; Evans, I.; Kern, A.; Parsons, S. The TOPAS Symbolic Computation System. *Powder Diffr.* **2011**, *26*, S22−S25.
(22) Evans, I.; Appel, M.; Gonzalez, M. A.; Koza, M. M.; Piovano, A.; Schwaighofer, B.Fluorite-type solid electrolytes with complex oxide ion diffusion mechanisms; Institut Laue-Langevin (ILL). https://doi.ill.fr/10.5291/ILL-DATA.7-03-184 (accessed Sept 30, 2022).
(23) Goodway, C.; McIntyre, P.; Sears, A.; Belkhier, N.; Burgess, G.; Kirichek, O.; Lelièvre-Berna, E.; Marchal, F.; Turc, S.; Wakefield, S. A Fast-Cooling Mode for Blue Series Furnaces. *J. Neutron Res.* **2020**, *21*, 137−142.
(24) Frick, B.; Combet, J.; Van Eijck, L. New Possibilities with Inelastic Fixed Window Scans and Linear Motor Doppler Drives on High Resolution Neutron Backscattering Spectrometers. *Nucl. Instrum. Methods Phys. Res., Sect. A* **2012**, *669*, 7−13.
(25) Arnold, O.; Bilheux, J. C.; Borreguero, J. M.; Buts, A.; Campbell, S. I.; Chapon, L.; Doucet, M.; Draper, N.; Ferraz Leal, R.; Gigg, M. A.; Lynch, V. E.; Markvardsen, A.; Mikkelson, D. J.; Mikkelson, R. L.; Miller, R.; Palmen, K.; Parker, P.; Passos, G.; Perring, T. G.; Peterson, P. F.; Ren, S.; Reuter, M. A.; Savici, A. T.; Taylor, J. W.; Taylor, R. J.; Tolchenov, R.; Zhou, W.; Zikovsky, J. Mantid—Data Analysis and Visualization Package for Neutron Scattering and MSR Experiments. *Nucl. Instrum. Methods Phys. Res., Sect. A* **2014**, *764*, 156−166.
(26) Kresse, G.; Furthmüller, J. Efficiency of Ab-Initio Total Energy Calculations for Metals and Semiconductors Using a Plane-Wave Basis Set. *Comput. Mater. Sci.* **1996**, *6*, 15−50.
(27) Kresse, G.; Joubert, D. From Ultrasoft Pseudopotentials to the Projector Augmented-Wave Method. *Phys. Rev. B: Condens. Matter Mater. Phys.* **1999**, *59*, 1758−1775.
(28) Perdew, J. P.; Burke, K.; Ernzerhof, M. Generalized Gradient Approximation Made Simple. *Phys. Rev. Lett.* **1996**, *77*, 3865−3868.
(29) Goret, G.; Aoun, B.; Pellegrini, E. MDANSE: An Interactive Analysis Environment for Molecular Dynamics Simulations. *J. Chem. Inf. Model.* **2017**, *57*, 1−5.
(30) Chudley, C. T.; Elliott, R. J. Neutron Scattering from a Liquid on a Jump Diffusion Model. *Proc. Phys. Soc.* **1961**, *77*, 353−361.
(31) Dunstan, M. T.; Halat, D. M.; Tate, M. L.; Evans, I. R.; Grey, C. P. Variable-Temperature Multinuclear Solid-State NMR Study of Oxide Ion Dynamics in Fluorite-Type Bismuth Vanadate and Phosphate Solid Electrolytes. *Chem. Mater.* **2019**, *31*, 1704−1714.
(32) Jakobsen, H. J.; Bildsøe, H.; Brorson, M.; Gan, Z.; Hung, I. Quantitative Dynamics and Structure for Crystalline Cs_2WO_4 and $KMnO_4$ Determined from High-Field ^{17}O Variable-Temperature MAS NMR Experiments. *J. Phys. Chem. C* **2014**, *118*, 20639−20646.
(33) Wilmer, D.; Feldmann, H.; Lechner, R. E. Ion Dynamics in Solid Solutions of Sodium Phosphate and Sodium Sulfate. *Phys. Chem. Chem. Phys.* **2002**, *4*, 3260−3265.
(34) Yang, X.; Fernández-Carrión, A. J.; Wang, J.; Porcher, F.; Fayon, F.; Allix, M.; Kuang, X. Cooperative Mechanisms of Oxygen Vacancy Stabilization and Migration in the Isolated Tetrahedral Anion Scheelite Structure. *Nat. Commun.* **2018**, *9*, 4484.
(35) Shannon, R. D. Revised Effective Ionic Radii and Systematic Studies of Interatomie Distances in Halides and Chaleogenides. *Acta Crystallogr., Sect. A* **1976**, *32*, 751−767.
(36) Wind, J.; Mole, R. A.; Yu, D.; Ling, C. D. Liquid-like Ionic Diffusion in Solid Bismuth Oxide Revealed by Coherent Quasielastic Neutron Scattering. *Chem. Mater.* **2017**, *29*, 7408−7415.
(37) Peet, J. R.; Fuller, C. A.; Frick, B.; Zbiri, M.; Piovano, A.; Johnson, M. R.; Evans, I. R. Direct Observation of Oxide Ion Dynamics in $La_2Mo_2O_9$ on the Nanosecond Timescale. *Chem. Mater.* **2017**, *29*, 3020−3028.
(38) Auckett, J. E.; Studer, A. J.; Pellegrini, E.; Ollivier, J.; Johnson, M. R.; Schober, H.; Miiller, W.; Ling, C. D. Combined Experimental and Computational Study of Oxide Ion Conduction Dynamics in $Sr_2Fe_2O_5$ Brownmillerite. *Chem. Mater.* **2013**, *25*, 3080−3087.
(39) Kuang, X.; Green, M. A.; Niu, H.; Zajdel, P.; Dickinson, C.; Claridge, J. B.; Jantsky, L.; Rosseinsky, M. J. Interstitial Oxide Ion Conductivity in the Layered Tetrahedral Network Melilite Structure. *Nat. Mater.* **2008**, *7*, 498−504.
(40) Hempelmann, R.*Quasielastic Neutron Scattering and Solid State Diffusion*; Oxford University Press, 2000.
(41) Morelon, N. D.; Kneller, G. R.; Ferrand, M.; Grand, A.; Smith, J. C.; Bée, M. Dynamics of Alkane Chains Included in an Organic Matrix: Molecular Dynamics Simulation and Comparison with Neutron Scattering Experiment. *J. Chem. Phys.* **1998**, *109*, 2883−2894.
(42) Peet, J. R.; Widdifield, C. M.; Apperley, D. C.; Hodgkinson, P.; Johnson, M. R.; Evans, I. R. Na^+ Mobility in Sodium Strontium Silicate Fast Ion Conductors. *Chem. Commun.* **2015**, *51*, 17163−17165.
(43) Esaka, T.; Mina-ai, T.; Iwahara, H. Oxide Ion Conduction in the Solid Solution Based on the Scheelite-Type Oxide $PbWO_4$. *Solid State Ionics* **1992**, *57*, 319−325.

https://doi.org/10.1021/acs.chemmater.2c03103
Chem. Mater. 2023, 35, 1125−1133

(44) Santibáñez-Mendieta, A. B.; Didier, C.; Inglis, K. K.; Corkett, A. J.; Pitcher, M. J.; Zanella, M.; Shin, J. F.; Daniels, L. M.; Rakhmatullin, A.; Li, M.; Dyer, M. S.; Claridge, J. B.; Blanc, F.; Rosseinsky, F.; Rosseinsky, M. J. $La_3Li_3W_2O_{12}$ Ionic Diffusion in a Perovskite with Lithium on Both A-and B-Sites. *Chem. Mater.* **2016**, *28*, 7833−7851.
(45) Kim, N.; Hsieh, C. H.; Huang, H.; Prinz, F. B.; Stebbins, J. F. High Temperature ^{17}O MAS NMR Study of Calcia, Magnesia, Scandia and Yttria Stabilized Zirconia. *Solid State Ionics* **2007**, *178*, 1499−1506.

https://doi.org/10.1021/acs.chemmater.2c03103
Chem. Mater. 2023, 35, 1125−1133